Surface-based registration between CT and US for image-guided percutaneous renal access – a feasibility study

João Gomes-Fonseca[1,2,#]; Sandro Queirós[1,2,3]; Pedro Morais[1,2,4]; António C.M. Pinho[5]; Jaime C. Fonseca[3,6]; Jorge Correia-Pinto[1,2,7]; Estêvão Lima[1,2,8]; João L. Vilaça[1,2,4].

[1]Life and Health Sciences Research Institute (ICVS), School of Medicine, University of Minho, Braga, Portugal;

[2]ICVS/3B's-PT, Government Associate Laboratory, Braga/Guimarães, 4710-057, Portugal;

[3]Algoritmi Center, School of Engineering, University of Minho, Guimarães, Portugal

[4]2Ai, Polytechnic Institute of Cávado and Ave, Barcelos, Portugal.

[5]Department of Mechanical Engineering, School of Engineering, University of Minho, Guimarães, Portugal;

[6]Department of Industrial Electronics, School of Engineering, University of Minho, Guimarães, Portugal;

[7]Department of Pediatric Surgery, Hospital of Braga, Braga, Portugal;

[8]Deparment of Urology, Hospital of Braga, Braga, Portugal;

#Corresponding author:

Life and Health Sciences Research Institute (ICVS)

School of Medicine - University of Minho

Campus de Gualtar, 4710-057, Braga, Portugal

Phone: +351 253 604 891

Email: joaofonseca@med.uminho.pt

Abstract

Purpose: Nowadays, the percutaneous renal access (PRA) is planned and guided by the independent evaluation of different pre- and intraoperative images, such as computed tomography (CT), ultrasound (US) imaging and fluoroscopy, notably increasing the difficulty of the intervention and requiring great operator expertise. As a crucial step in accessing the kidney in several minimally invasive interventions, PRA practicality and safeness may be improved through the fusion of CT and US data. Therefore, this work aims to assess the potential of an enhanced image-guided framework to PRA by fusion the US and CT data through a surface-based registration technique.

Methods: Ten porcine kidney phantoms with fiducial markers were imaged using CT and 3D US. Both images were manually segmented and aligned to create a ground-truth. In a virtual simulated and controlled environment, 2D contours were extracted by slicing the 3D US kidney surfaces from a single-oriented acquisition and using usual PRA US-guided views, while the 3D CT kidney surfaces were misaligned to simulate positional variability. The surface-based registration was assessed using two state-of-the-art methods of the iterative closest point algorithm (*point-to-point*, ICP1; and *point-to-plane*, ICP2) and three hypotheses were studied: i) use of single-plane (transverse view, SP_T; and longitudinal view, SP_L) *versus* bi-plane imaging (BP); ii) use of multiple planes acquired by an US probe's sweep; and iii) influence of US probe's sweep movements during acquisition.

Results: SP_L and BP acquisitions had the best performance when multiple planes and ICP2 method were used. The average point-to-point distance between registered US and ground-truth surfaces for SP_L and BP were 2.47 mm and 2.48 mm, respectively. Focusing on the US probe's sweep movements, a large sweep along the central longitudinal view presented the best results for SP_L, with an average point-to-point distance of ~2 mm.

Conclusions: This is the first study that assesses the optimal 2D US acquisition protocol to improve surface-based registration between CT and US data for image-guided PRA. Therefore, multiple slices and specific sweep movements may be crucial to improve final registration. Surface-based registration is here suggested as a valid strategy for intraoperative image fusion using CT and US data. This strategy has the potential to be applied to different image modalities and interventions, and the presented methodology has the potential to be used to assess their feasibility.

Keywords: Image-guided interventions; percutaneous renal access; ultrasound; computed tomography; surface-based registration.

1 INTRODUCTION

Percutaneous renal access (PRA) is a surgical step where the surgeon inserts a surgical needle from the skin until the kidney target site. It is used in several minimally invasive kidney interventions (MIKI), such as percutaneous nephrolithotomy, kidney radiofrequency ablation of renal tumors, and kidney biopsies. During MIKI, medical imaging is crucial in two distinct phases: the surgical planning, which usually relies on preoperative computed tomography (CT) data; and the PRA, which is generally performed under intraoperative imaging guidance [1,2]. Fluoroscopy and two-dimensional (2D) ultrasound (US) are the most common modalities for PRA, providing a real-time depiction of the renal system and instruments. However, since fluoroscopy requires radiation exposure, pure US image guidance appeared, recently, as a potential and attractive solution. Besides avoiding radiation, US has been shown to present other advantages over fluoroscopy, including shorter puncture time, higher success rate of first puncture, less blood loss, and fewer complications [3].

The surgeon's ability to visualize and reach the anatomical target during PRA delimits the MIKI success. The ideal PRA is one that allows a safe and precise access to the kidney target site while minimizing bleeding. Therefore, PRA remains a challenging task for surgeons [4]. Inaccurate and multiple needle punctures often cause complications [1,5], where injuries to kidney or contiguous organs can eventually prejudice the surgical outcome.

To overcome the abovementioned drawbacks, many paths and technological advances have been proposed to improve PRA [6]. Recently, PRA was performed with excellent results using ureteroscopy and an electromagnetic tracking system [7,8]. However, the authors mentioned the lack of visualization of anatomical structures in real-time during puncturing as an important disadvantage. In the past few years, concepts of enhanced image-guided interventions (eIGI) have been studied for PRA. eIGI are computer-

based systems that overlap different imaging data to improve the physicians' perception of the target site. In this sense, anatomical information from preoperative images - such as CT or magnetic resonance imaging (MRI) – are fused with real-time intraoperative US images, allowing to enhance the latter with preoperative planning information [9–16].

One of the fundamental steps of eIGI is the registration between the preoperative and intraoperative image data, bringing them to the same coordinate system. Several registration methods have been presented in the literature for eIGI, including landmark-based, intensity-based and segmentation-based methods [17–19]. Despite the primacy of intensity-based registration methods in the past few years [18], segmentation-based followed by surface alignment has been shown to be more successful than landmark-based and intensity-based when the images present low quality or missing data [19]. Moreover, surface-based alignment methods are computationally attractive solutions, because they become independent of the image after segmentation and, usually, reduce the number of data under processing.

Previous works have tried to fuse 2D US with preoperative data for MIKI based on surface-based registration. Ahmad *et al.* proposed to individually segment arbitrarily placed and oriented US slices using an optical tracker coupled to a laparoscopic US probe [20]. Based on the spatial location of the US probe, the three-dimensional (3D) surface of a kidney tumor phantom is reconstructed using two different segmentation approaches. Differences were measured after registration of the reconstructed surfaces with the ideal reference, corroborating the added-value of this strategy. Mozer *et al.* used multiple and sparse transverse and longitudinal contours to align US and CT data [13]. Li *et al.* used two pairs of orthogonal US slices to register with a MRI model [12]. In addition, the authors presented a respiratory gating technique to compensate organ motion. The same authors presented a different approach based on statistical shape model, which was used to reconstruct kidney surfaces using sparse points from US

images [14]. Finally, Seo *et al.* used two orthogonal 2D US probes to create a bi-plane US imaging of the kidney and, then, estimate the pose of a preoperative 3D model [21]. The proposed method showed high accuracy and robustness, being tested in different applications [22–24]. Overall, the previous works demonstrated that surface-based registration allows to achieve good results. However, most of them acquired 2D US images from arbitrary and sparse longitudinal and transverse views, using different strategies to maintain continuous and feasible registration, as respiratory gating, a simultaneous acquisition using two US probes, and robot motion compensation, which are not always accurate and practical to perform within the operating room.

Due to the improvements in real-time image processing, namely in segmentation [25], in tracking [26], and in general computational capabilities [27,28], the continuous registration and monitoring of medical images is now possible. Notwithstanding, imaging should also be continuous to perform continuous organ monitoring. Since the direct access to online US raw data is restricted by most manufacturers, the usual approach is to grab the real-time data displayed on the screen, being therefore restricted to a 2D image view. Taking this into account, this work aims to assess the accuracy of surface-based registration between CT and 2D US images for image-guided PRA. Thus, this work intends to answer three practical hypotheses:

- *Hypothesis 1*: Can the use of bi-plane slices from four-dimensional (4D) probes (orthogonal images), when compared to 2D probes, benefit the registration between US and CT kidney surfaces?
- *Hypothesis 2*: Can the use of multiple slices (acquired by sweeping the probe) benefit the registration between US and CT kidney surfaces?
- *Hypothesis 3*: Can different US probe's sweep movements (acquiring kidney slices at different positions) benefit the final alignment between US and CT kidney surfaces?

This paper is structured as follows. In section 2, we present our experimental setup, which is based on phantoms manufactured for CT and US imaging for image-guided PRA. Additionally, we present our experimental design, which explains how the manually segmented 3D phantom models from CT and US are used to virtual simulate 2D US acquisitions in a controlled environment, as well as describes the different registration methods used in the assessment. In section 3, we present the results, which are discussed in section 4. In section 5, we present the main conclusions of our study.

2 MATERIALS AND METHODS

2.1 Experimental setup

2.1.1 Phantom preparation

Phantoms were constructed using the protocol presented in Gomes-Fonseca *et al.* [29]. In short, the phantom was manufactured based on a porcine kidney combined with tissue mimicking material (TMM) and implanted fiducial markers (FMs), see Figure 1-A. While the TMM mimics the surrounding tissues of the kidney, the FMs are used to accurately align both US and CT images (Figure 1-B). Overall, ten phantoms were built.

2.1.2 Image acquisition

The CT images were acquired using a Philips Brilliance 64 CT scanner (Philips Healthcare, Best, The Netherlands). The X-ray tube current and peak voltage were set to 313 mA and 120 kV, respectively. The abdomen protocol was selected. On average, the CT volume size was 512x512x300 with a voxel resolution of $0.701 \times 0.701 \times 1$ mm.

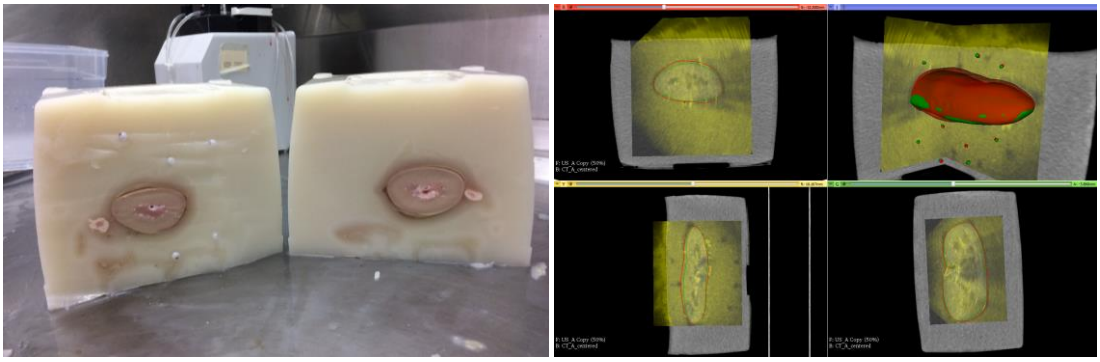

A B

Figure 1 – (A) A porcine kidney phantom model with implanted fiducial markers (FMs). The image represents the phantom cut in half. (B) Ground-truth. Images and segmented surfaces from both CT and US volumes of a kidney phantom model. Images are aligned based on selected (FMs). CT images, surfaces and associated FMs are represented by gray level images, green surfaces and points, respectively, while yellow and red are used to represent US images, surfaces and points.

The US images were acquired using a Voluson P6 US system (GE Healthcare, Milwaukee, Wisconsin, USA). The 4D convex abdominal transducer (RAB2-6-RS, 2-5 MHz) was used. According to the machine settings, 3D images were acquired using the high-quality mode (setting: high2), the maximum field-of-view (setting: B90º/V85º) and a depth of 15.9 cm. The voxel resolution was 0.667×0.667×0.667 mm with a volume size of 235×172×197.

2.2 Experimental design

2.2.1 Data preparation

Two segmented 3D surfaces were initially created for each phantom, namely one using the CT images, and another based on the US images. In detail, the CT volume was delineated using the 3D Slicer software (version 4.6). The files from the 3D US system were initially converted to Meta Image files using BabyOSlice software (Tomovision, Canada), and were then uploaded to the 3D Slicer software and manually delineated. In both cases, the manual delineation relied on multiple 2D contours followed by 3D interpolation to obtain the final 3D surface.

In addition, the implanted FMs were manually detected on both CT and US volumes of each phantom (Figure 1). Note that the FM are visible as brighter and darker structures in US and CT images, respectively. The detected FMs were then aligned based on the strategy presented by Horn *et al.* [30] (using the image-guided therapy toolbox available on 3D Slicer), establishing the ground-truth alignment between both surfaces.

2.2.2 Data simulation

To virtually simulate the normal variability found throughout an intervention, both in terms of US field-of-view and anatomical kidney positioning, the experimental data was simulated in two independent stages: 1) simulation of the variability associated with the probe position/orientation wrt. the patient's body in the operative room (section 2.2.2.A); and 2) simulation of the anatomical positional variability of the preoperative data (section 2.2.2.B).

A. Simulation of intraoperative kidney acquisition and segmentation of 2D US images

According to Chu *et al.* [31], during US-guided PRA, the US probe is typically positioned to capture longitudinal and/or transverse sections of the kidney (Figure 2). Thus, in these experiments, the kidney's central *longitudinal* and *transverse* sections were defined, per convention, to be aligned with the *xz* and *xy planes*, respectively (Figure 3-A). The US probe was virtually positioned 6 cm away from the center of the kidney US surface, mimicking the typical distance between kidney and skin [31], and the center of rotation defined at the probe's tip (Figure 2).

Multiple 2D US slices and their respective 2D contours were generated by reformatting the original volume and surface. In this sense, multiple rotations (i.e., *roll*, *pitch*, and *yaw*) of the central *longitudinal* and *transverse* planes (Figure 3-A) were applied. Henceforth, the rotations linked to US imaging will be designated as $roll_{US}$, $pitch_{US}$,

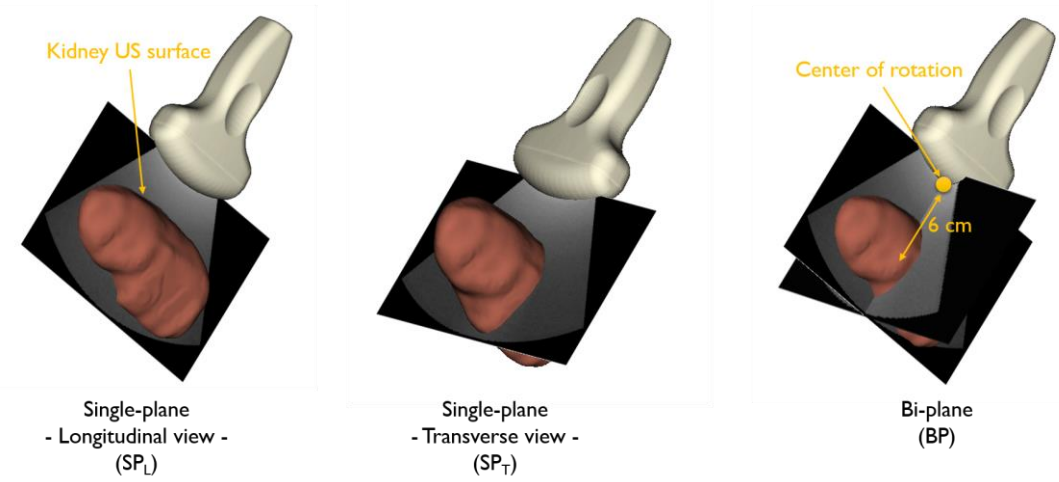

Figure 2 – Representation of single-plane acquisition for *longitudinal* (SP_L) and *transverse* (SP_T) *views*, and bi-plane (BP) for *both* views in a virtual simulated and controlled environment. Surface-based registration for image-guided percutaneous renal access is assessed based on these probe views. A single-oriented acquisition fixed on the center of rotation is performed, mimicking a continuous imaging of the kidney.

and yaw_{US}, each representing a different simulated probe sweep movement and respective 2D contours wrt. the kidney.

B. Simulation of preoperative CT kidney surfaces' positional variability

The anatomical positional variability expected before surface-based registration was simulated by applying transformations to the CT surface. The idea is to mimic the different orientations that the kidney can have before the fusion, which affect the initial alignment between modalities. These differences are usually related to the patient's body positioning during preoperative and intraoperative acquisitions. As performed above, changes in *roll*, *pitch*, and *yaw* orientations were applied wrt. the CT kidney surfaces' center. The different orientations were applied in pairs following the Euler convection (*yaw-pitch-roll*), namely *pitch-roll*, *yaw-roll*, and *yaw-pitch.* This split intended to simplify the evaluation, while maintaining a complex misalignment between volumes. Nineteen rotations were performed per orientation, ranging from -90º to 90º with 10º increments. Each pair created 361 misaligned surfaces, in a total of 1083 per phantom. Then, to simplify the results' interpretation, pairs with equal changes in

orientation were combined. Henceforth, changes in orientation of the CT surfaces are termed as $roll_{CT}$, $pitch_{CT}$, and yaw_{CT}.

2.2.3 Registration algorithms

The tests were performed assuming rigid transformation models between surfaces. The iterative closest point (ICP) algorithm was used to estimate point correspondences between point clouds and compute the optimal transformation between them [32–34]. Usually, ICP is a fast technique, which is very important for image-guided interventions. In this work, two state-of-the-art variants of *error metric* were used:

1) the *point-to-point* error metric that sums the squared distances of source points to target points:

$$\boldsymbol{R}, \boldsymbol{t} \leftarrow \underset{\boldsymbol{R},\boldsymbol{t}}{\arg\min} \sum_{i=1}^{N} \|(\boldsymbol{R}\boldsymbol{p}_i + \boldsymbol{t}) - \boldsymbol{q}_i\|^2 \quad (1)$$

where $\boldsymbol{p}_i$ is a source point and $\boldsymbol{q}_i$ a corresponding point in the target point cloud, while $\boldsymbol{R}$ is the rotation matrix and $\boldsymbol{t}$ is the translation vector that minimizes the distance between source and target. A closed form solution for the minimization of the *point-to-point* error metric is the Singular Value Decomposition (SVD) algorithm [35,36]. Henceforward, this variant is termed ICP1.

2) and, the *point-to-plane* error metric that sums the distances of source points to the surface normal in which the matched target points reside:

$$\boldsymbol{R}, \boldsymbol{t} \leftarrow \underset{\boldsymbol{R},\boldsymbol{t}}{\arg\min} \sum_{i=1}^{N} \left\| \left((\boldsymbol{R}\boldsymbol{p}_i + \boldsymbol{t}) - \boldsymbol{q}_i \right) \cdot \boldsymbol{n}_i \right\| \quad (2)$$

where $\boldsymbol{n}_i$ denotes the estimated surface normal at $\boldsymbol{q}_i$. The only closed form solution for the minimization of the *point-to-plane* error metric is after linearization of the rotation matrix [35,36]. Henceforward, this variant is termed ICP2.

Finally, throughout these experiments, the CT surface was defined as the target point cloud, with the US surface being the source point cloud. For both variants, a fixed number of iterations were applied (25 iterations were used in the current experiments).

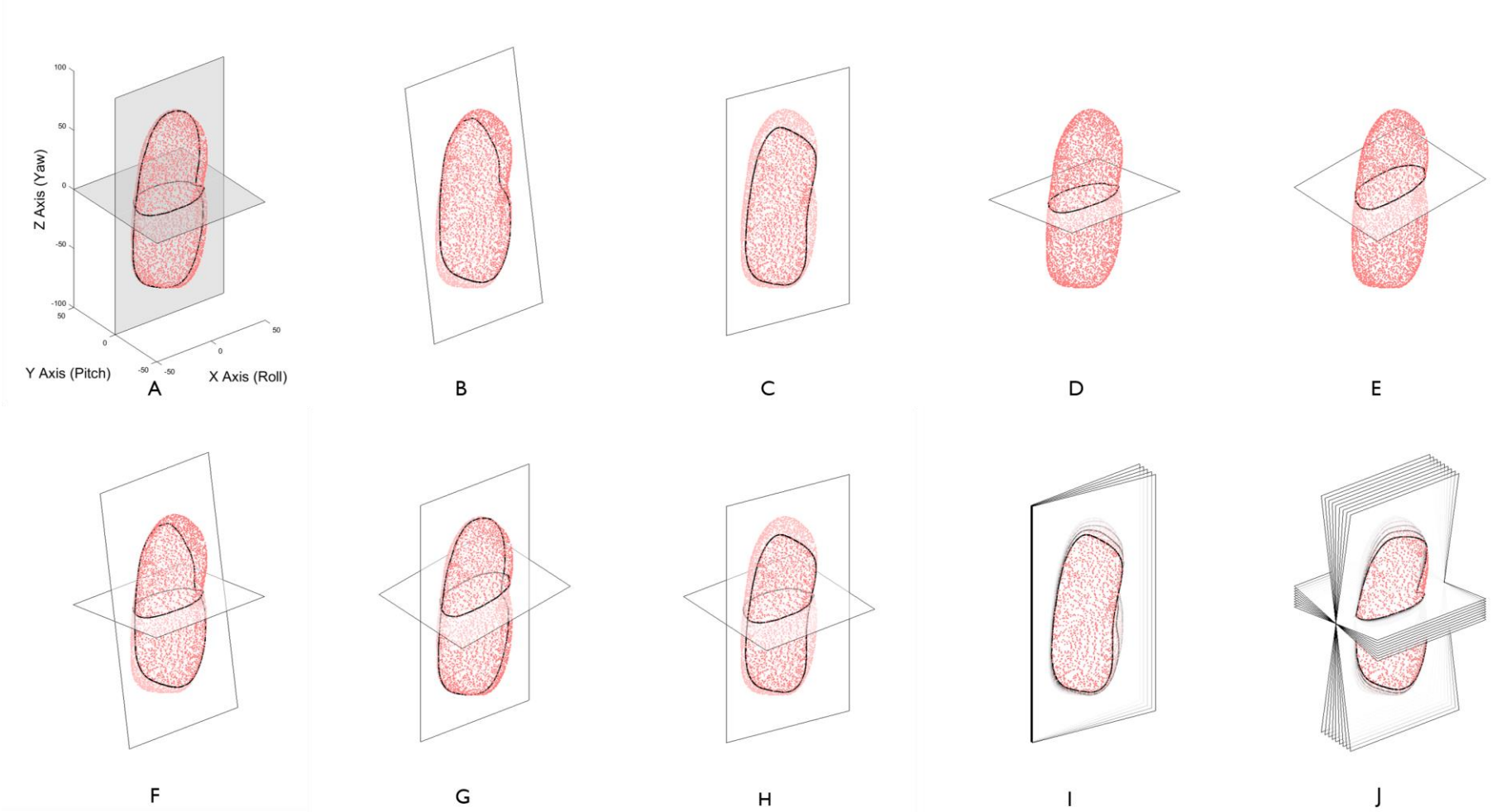

Figure 3 – Examples of kidney slicing simulation. (A) Central *longitudinal* and *transverse* views. SP_L rotated in (B) $roll_{US}$, and (C) yaw_{US} (rotation: -10º). SP_T rotated in (D) $roll_{US}$, and (E) $pitch_{US}$ (rotation: -10º). BP rotated in (F) $roll_{US}$, (G) $pitch_{US}$, and (H) yaw_{US} (rotation: -10º). (I) SP_L using multiple slices in yaw_{US} (5 slices). (J) BP using multiple slices in $roll_{US}$ (9 slices). All images were captured with the same view.

2.2.4 Experiments

The experiments were designed focused on the three abovementioned hypotheses:

Hypothesis 1 was performed by testing the registration performance of *longitudinal* and *transverse* slices (single-plane acquisitions), as well as the case in which *both* slices are used together (bi-plane acquisitions). These two options test the use of both 2D and 4D US probes, simulating the grabbing of the real-time data displayed on the screen (as the direct access to online US raw data is restricted). To simplify the reading, single-plane acquisitions from longitudinal slices will be designated as SP_L; single-plane acquisitions from transverse sections as SP_T; and bi-plane acquisitions as BP.

Hypothesis 2 attempted to verify if multiple and sparse contours of the kidney, obtained by sweeping the probe from a single-oriented acquisition, can improve the registration between US and CT kidney surfaces.

Hypothesis 3 attempted to verify if different movements of the US probe during an acquisition can improve the registration between US and CT kidney surfaces. According to the US probe's center of rotation, $roll_{US}$, $pitch_{US}$, and yaw_{US} simulate different movements that differently slice the kidney.

Since these three hypotheses are intrinsically linked, different parameters were varied together. Thus, SP_L, SP_T, and BP were transformed using their central planes as references. Therefore, -10º to 10º with increments of 2.5º were used along the $roll_{US}$, $pitch_{US}$, and yaw_{US} orientations. Each slice originated a specific contour. Moreover, these contours were sequentially combined in sets of one, two, five or nine contours. Finally, each set of contours was registered against all *misaligned CT surfaces* for each phantom. Furthermore, the experiments tested both variants of the ICP algorithm.

It is important to mention that SP_L originates different contours when changing $roll_{US}$ and the yaw_{US} (Figures 3-B and 3-C), while SP_T the $roll_{US}$ and the $pitch_{US}$ (Figures 3-D

and 3-E). Similarly, BP originates different contours when changing $roll_{US}$, $pitch_{US}$, and yaw_{US} (Figures 3-F, 3-G and 3-H).

2.3 Error metrics and statistical analysis

As abovementioned, FMs were used to establish the *ground-truth alignment* between CT and US images. In this sense, the fiducial registration error (FRE) describes the error inherently associated with the ground-truth itself. During experiments, all applied transformations (sections 2.2.2.A and 2.2.2.B) assumed the *ground-truth alignment* as the reference position.

Next, to assess the errors after registration, two surfaces were used, namely the *misaligned CT surfaces* and the *misaligned US surfaces*. Both surfaces were equally rotated applying the transformations described in section 2.2.2.B. While the *misaligned CT surface* represents the errors between image modalities, the *misaligned US surface* represents the ground-truth position that should be found upon the registration process. Indeed, the registration process computes the transformation from US contours (from section 2.2.2.A) to the *misaligned CT surface*, and then this transformation is used to obtain the *registered US surface.*

All metrics were computed using the 3D surfaces and volumes. Therefore, the average distance (AVD), the Hausdorff distance (HD), and the Dice similarity coefficient (DSC) were used to measure the differences between *misaligned CT surface* and *registered US surface*, whereas the average point-to-point distance (P2P) and maximum angle error (MAE) measured the differences between the *misaligned US surface* and *registered US surface*. The performance was assessed by comparing the error metrics (AVD, HD, DSC, P2P, and MAE) across different scenarios.

All statistical tests were conducted using MATLAB® (version R2016b, The Mathworks Inc., Natick, MA). The assumption of normality was assessed for all variables and,

according to the results, parametric or nonparametric tests were applied accordingly. The effect size and statistical significance were reported. All statistics were considered significant if $p < 0.05$.

3 RESULTS

3.1 General observations

Due to the non-normal distribution of the computed metrics, all results are presented using the median and the interquartile range (IQR). Moreover, non-parametric statistical tests were performed to compare different scenarios.

All ten phantoms were successfully produced and imaged. These models were aligned using the correspondent FMs selected on both images. On average, FRE was 0.98 (0.21) mm, indicating a close alignment between US and CT images and validating the ground-truth used. Respectively, DSC, AVD, and HD were 90.40 (4.16) %, 1.77 (0.28) mm and 4.83 (1.41) mm, reinforcing the high accuracy of this stage.

3.2 *Hypothesis 1*

SP_L and BP revealed better performance than SP_T during surface-based registration. Respectively, the average P2P distance for SP_L, SP_T and BP was 8.09 (8.34) mm, 27.10 (22.61) mm, and 6.30 (8.15) mm using ICP1; and 8.41 (40.53) mm, 41.84 (32.55) mm, and 3.77 (2.79) mm using ICP2 (1 slice, see Table 1). The differences between SP_L, SP_T and BP were statistically significant for both ICP methods ($p < .001$). Pairwise comparisons revealed that all groups were statistically different ($p < .05$).

Table 1 – Results of multiple slices acquisitions using *Longitudinal* (SP_L), *Transverse* (SP_T) and *Both* (BP) views. Two iterative closest point methods are presented (ICP1 – point-to-point error metric; ICP2 – point-to-plane error metric), and five different metrics are computed. Dice similarity coefficient (DSC); average distance (AVD); 95th Hausdorff distance (HD); average point-to-point distance (P2P); and maximum angle error (MAE). All metrics are represented by median (IQR), being the statistical test performed also indicated. Best values are in bold. *Pairs of slices.

	DSC (%)		*AVD (mm)*		*HD (mm)*		*P2P (mm)*		*MAE (degrees)*	
	ICP 1	**ICP 2**	**ICP 1**	**ICP 2**	**ICP 1**	**ICP 2**	**ICP 1**	**ICP 2**	**ICP 1**	**ICP 2**
SP_L										
1. *1 slice*	81,18 (12,21)	80,10 (19,19)	3,52 (2,18)	3,67 (3,42)	8,52 (4,73)	8,80 (7,57)	8,09 (8,34)	8,41 (40,53)	12,77 (13,34)	11,64 (74,33)
2. *2 slices*	82,65 (10,57)	84,46 (15,55)	3,24 (1,89)	2,84 (2,64)	7,80 (4,16)	7,36 (5,85)	7,20 (7,77)	6,26 (40,65)	11,85 (13,48)	9,06 (66,38)
3. *5 slices*	86,91 (7,95)	88,54 (6,52)	2,39 (1,49)	2,01 (1,04)	5,81 (3,19)	5,09 (2,47)	4,86 (6,77)	3,42 (39,52)	8,66 (13,68)	4,58 (10,61)
4. *9 slices*	88,06 (7,24)	**90,62 (4,59)**	2,13 (1,31)	**1,80 (0,69)**	4,91 (2,85)	**4,22 (2,27)**	4,02 (6,81)	**2,47 (3,36)**	6,73 (12,99)	**2,99 (5,54)**
SP_T										
5. *1 slice*	54,12 (21,82)	42,85 (17,58)	9,73 (6,29)	12,70 (7,85)	25,28 (18,04)	32,22 (19,33)	27,10 (22,61)	41,84 (32,55)	39,21 (25,22)	52,63 (48,26)
6. *2 slices*	54,57 (21,88)	45,31 (20,32)	9,62 (6,30)	12,15 (7,81)	24,97 (18,01)	30,93 (19,28)	26,66 (22,12)	39,48 (32,48)	38,79 (24,57)	48,73 (48,43)
7. *5 slices*	57,14 (23,29)	52,89 (28,76)	8,95 (6,57)	9,94 (8,17)	23,34 (18,43)	25,81 (19,23)	24,92 (22,24)	28,40 (32,47)	36,52 (23,60)	38,04 (47,76)
8. *9 slices*	60,74 (25,42)	63,62 (32,19)	7,91 (6,79)	6,84 (8,44)	20,64 (18,90)	19,52 (21,10)	23,12 (23,62)	21,49 (32,83)	33,87 (27,79)	26,32 (41,29)
BP										
9. *1 slice**	85,36 (9,48)	88,77 (5,84)	2,68 (1,77)	2,01 (0,93)	6,41 (4,07)	4,97 (2,08)	6,30 (8,15)	3,77 (2,79)	10,45 (15,15)	4,71 (5,65)
10. *2 slices**	85,87 (8,57)	89,32 (5,41)	2,57 (1,57)	1,97 (0,69)	6,03 (3,58)	4,84 (1,50)	5,75 (7,14)	3,45 (2,27)	9,53 (14,13)	4,38 (4,70)
11. *5 slices**	87,27 (7,44)	89,67 (4,47)	2,34 (1,37)	1,81 (0,61)	5,23 (2,90)	4,32 (1,39)	4,74 (6,50)	2,54 (1,87)	8,11 (13,59)	3,04 (3,86)
12. *9 slices**	87,81 (7,44)	**90,71 (4,14)**	2,24 (1,34)	**1,72 (0,63)**	4,88 (2,83)	**4,13 (1,40)**	4,37 (6,60)	**2,48 (2,03)**	7,26 (14,08)	**2,59 (4,10)**
Kruskal-wallis test *df = 11, N = 303240*	X^2(df,N) = 143988.5 p < .001, η^2 = 0.4748, All groups, p < .05, Except: 5-6, 4-12	X^2(df,N) = 172749.9 p < .001, η^2 = 0.5697, All groups, p < .05 Except: -	X^2(df,N) = 143969,8 p < .001, η^2 = 0.4748, All groups, p < .05, Except: 5-6	X^2(df,N) = 180478,6, p < .001, η^2 = 0.5952, All groups, p < .05, Except: 4-11	X^2(df,N) = 156872,4 p < .001, η^2 = 0.5173, All groups, p < .05, Except: 5-6, 4-12	X^2(df,N) = 186115,7 p < .001, η^2 = 0.6138, All groups, p < .05, Except: 4-11	X^2(df,N) = 89171,7 p < .001, η^2 = 0.2941, All groups, p < .05, Except: 5-6, 3-11	X^2(df,N) = 107939,4 p < .001, η^2 = 0.3560, All groups, p < .05, Except: 3-9, 4-11	X^2(df,N) = 86326,1 p < .001, η^2 = 0.2847, All groups, p < .05, Except: 5-6, 3-12	X^2(df,N) = 110811,6 p < .001, η^2 = 0.3654, All groups, p < .05, Except: 5-6, 4-11

3.3 *Hypothesis 2*

Table 1 summarizes the results obtained when using multiple slices. The results show that errors decrease when the number of slices used increases in SP_L, SP_T and BP ($p < .001$). This fact was observed in all metrics and in both ICP methods.

The lowest errors were obtained when nine slices were used to create a sparse 3D model of the kidney, with the ICP2 method being used. It is important to highlight that similar errors were obtained by SP_L and BP. Indeed, median values of DSC, AVD, HD, P2P and MAE were respectively 90.71%, 1.72 mm, 4.13 mm, 2.48 mm and 2.59º for

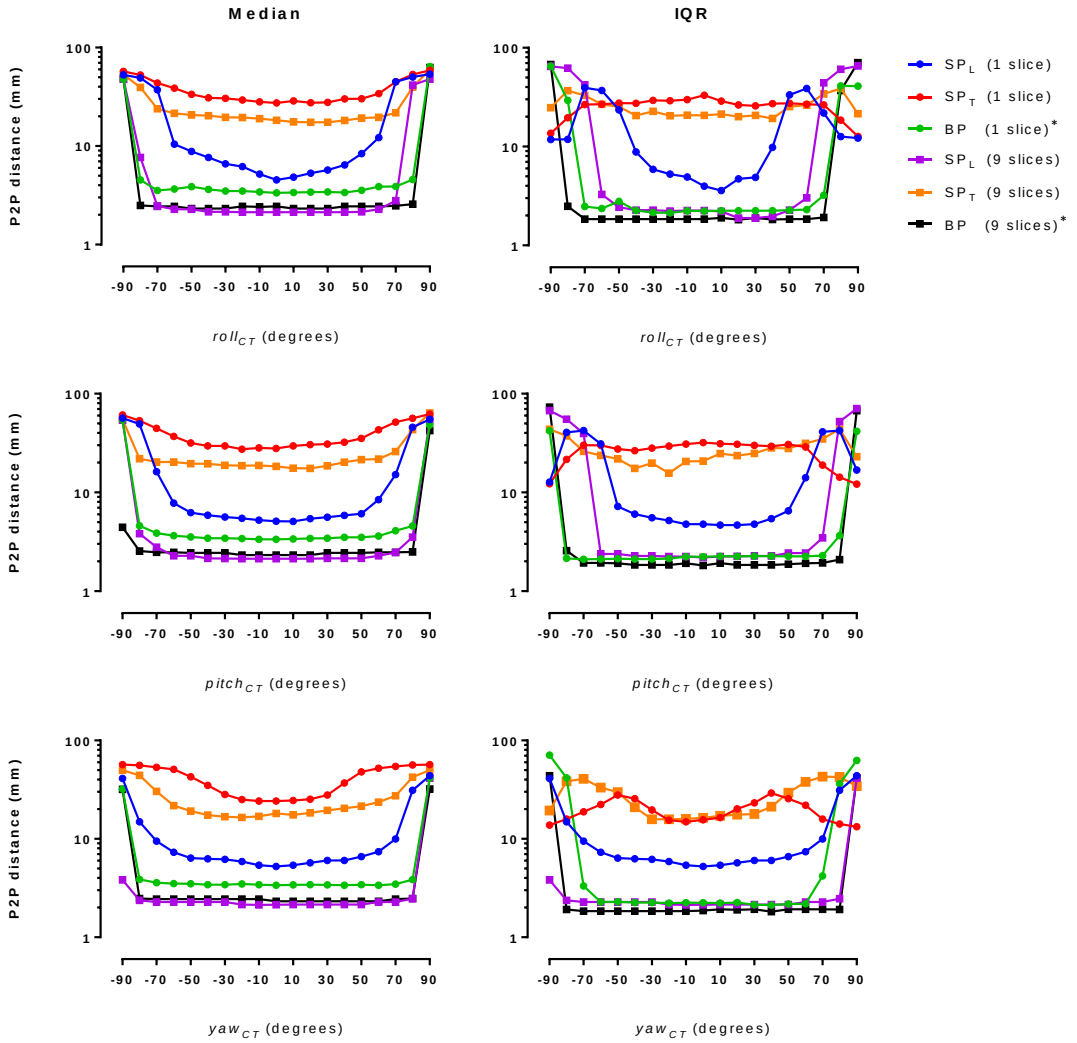

Figure 4 – Results of ICP2 method for one and nine slices acquisitions wrt. different CT misalignments. A line graph is used to represent the average P2P distance for each CT model misalignment. Each dot symbol illustrates the median/IQR value of all registrations. Lines represent different views used (SP_L, SP_T, and BP). Left graphs: Median values. Right graphs: Interquartile range (IQR) values. *Pairs of

328 BP, and 90.62%, 1.80 mm, 4.22 mm, 2.47 mm and 2.99º for SP_L. In addition, both
329 variants presented similar DSC, AVD, and HD errors when compared to the ground-
330 truth (section 3.1).

331 Figure 4 presents the median and IQR of average P2P distance for each angle applied
332 to misalign the CT model, i.e. $roll_{CT}$, $pitch_{CT}$, and yaw_{CT}. These graphs describe the
333 errors for SP_L, SP_T and BP, when using either one or nine slices for surface-based
334 registration. SP_L and BP had the best registration performance when 9 slices were
335 used. Misalignments over ± 50º on the CT surface were typically associated with higher
336 errors.

3.4 *Hypothesis 3*

Considering the previous results, Figure 5 shows the influence of different US probe movements ($roll_{US}$, $pitch_{US}$, and yaw_{US}) when SP_L and BP acquisitions with 9 slices were used. The results revealed that using yaw_{US} movements together with a SP_L acquisition presented lower errors, independently of the CT kidney orientation (i.e. for different CT misalignments, namely $roll_{CT}$, $pitch_{CT}$, and yaw_{CT}). Close values were obtained for the BP acquisition. However, BP presented lower IQR values, showing

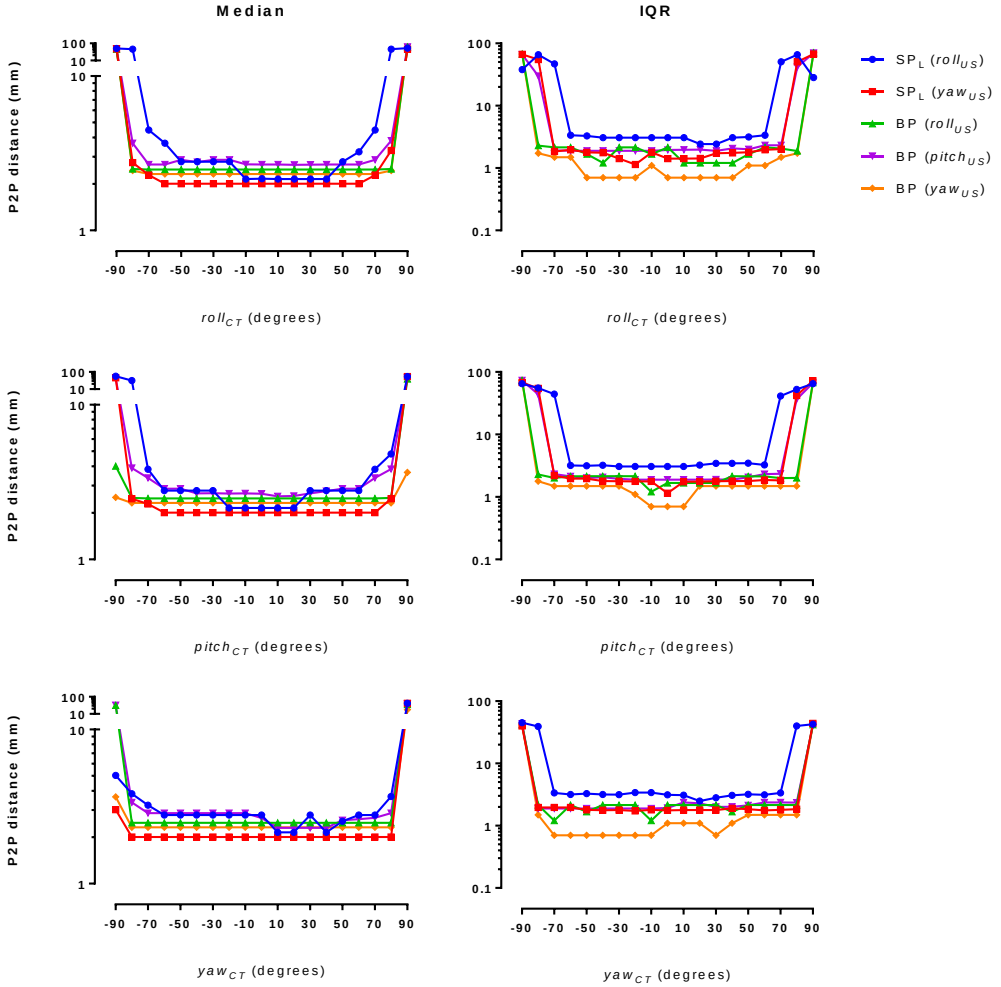

Figure 5 - Results for different US sweep probe movements ($roll_{US}$, $pitch_{US}$, and yaw_{US}) applied for both SP_L, and BP views. Graphs show results of using 9 slices for ICP2 method. Lines graphs with average P2P distance associated to each CT model misalignments. Each dot symbol illustrates the median/IQR value of all registrations. Left graphs: Median values. Right graphs: Interquartile range (IQR) values.

lower variability. The $pitch_{US}$ movement together with BP acquisition presented the worst results.

Due to the positive results of yaw_{US}, this US probe's sweep movement was further explored by capturing different zones of the kidney. Figure 6 describes the results of sweeping the kidney in different extremes using yaw_{US} movements, dividing them into a set of slices. The median differences between BP and SP_L were small, being slightly better for SP_L in Set2 and Set3. The lowest median values were obtained with the central set (i.e. Set3) for both BP and SP_L. In addition, the minimum values were obtained when the central longitudinal slices were captured (i.e. Set2, Set3, and Set 4). Again, BP presented a lower variability than SP_L.

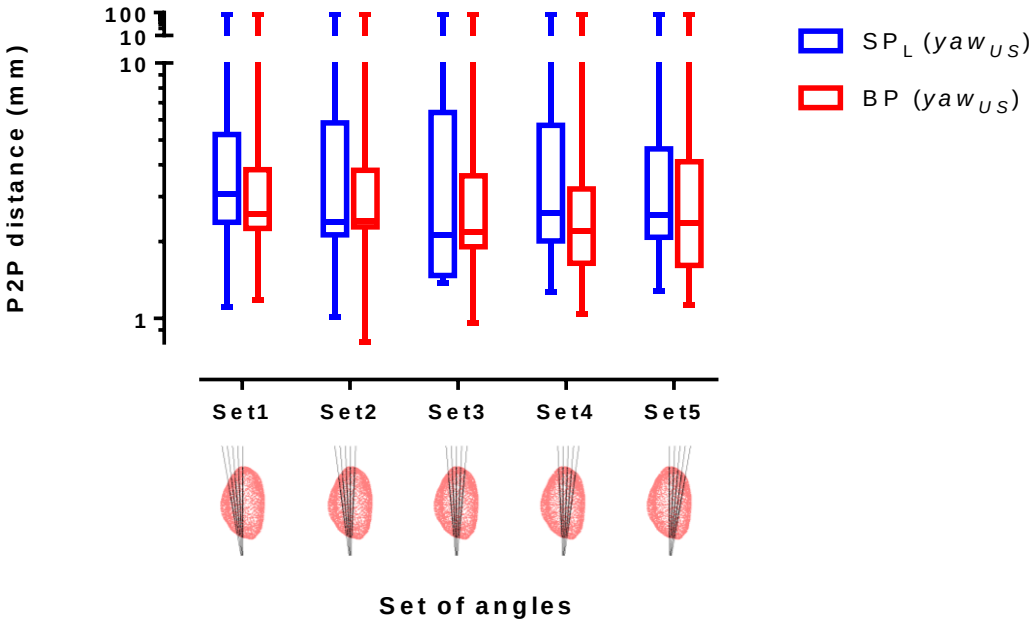

Figure 6 - Results of using yaw_{US} movement during 2D US acquisition for SP_L and BP. Boxplots show the results for different set of slices according to different slicing angles, namely Set1: [-10º -7.5º -5º -2.5º 0º]; Set2: [-7.5º -5º -2.5º 0º 2.5º]; Set3: [-5º -2.5º 0º 2.5º 5º]; Set4: [-2.5º 0º 2.5º 5º 7.5º]; Set5: [0º 2.5º 5º 7.5º 10º]. Set1 and Set5 represent the extremes of slicing, while Set3 the central one. Each set is represented by top views with the corresponding slices. Boxplots represent de minimum, first quartile, median, third quartile, and maximum of the P2P distance.

4 DISCUSSION

In this work, we studied the feasibility of two surface-based registration approaches for fusing 2D US and CT data to facilitate PRA procedures. The different approaches were tested using kidney phantom models and hundreds of thousands of surface-based registrations were performed, allowing an accurate evaluation of the algorithm's performance. In addition, manual segmentation of both image modalities simulated common differences between US and CT segmentation methods. This detail reinforces the results obtained in the present work since these differences demanded more from the registration process. To the best of our knowledge, this is the first study that assesses the optimal 2D US acquisition protocol to improve surface-based registration between 2D US and CT data for image-guided PRA. Thereby, three hypotheses were studied.

Hypothesis 1 with the question: "*Can the use of bi-plane slices from 4D probes (orthogonal images), when compared to 2D probes, benefit the registration between US and CT kidney surfaces?*", revealed that, globally, bi-plane acquisitions had better performance during surface-based registration. This is expected since more details of the kidney anatomy are captured (i.e. orthogonal images are acquired), which ultimately enhances the performance of the ICP method to automatically align intraoperative and preoperative spaces. Overall, the method performance is comparable to other state-of-the-art solutions using a similar orthogonal US images acquisition approach. *Seo et al.* reported an error of 1.68 mm in one phantom model (with biplane acquisition at the surface's center using two orthogonal 2D probes), and our study obtained an error of 2.01 mm (AVD for 1 slice BP, see Table 1) with higher anatomical variability. Moreover, it is relevant to mention that our initial ground-truth error between preoperative CT surface and intraoperative US surface was, on average, 1.77 mm (based on FMs), while Seo *et al*. assumed as gold-standard the registration of the preoperative surface with multiple biplane US contours. The concept of real-time

biplane US imaging has been also used in other medical fields, particularly in cardiology, with good outcomes. Lang *et al.* evaluated the accuracy and robustness of a surface-based registration method for intraoperative use. They found that the use of bi-plane contours had the best accuracy wrt. other approaches, with registration errors lower than 5 mm, even in clinical data [37]. The same authors also showed the potential of surface-based registration use in real-time image-guidance [38].

Considering in more detail Hypothesis 2: *"Can the use of multiple slices (acquired by sweeping the probe) benefit the registration between US and CT kidney surfaces?",* it was possible to observe a superior performance of the registration method when multiple slices were used. SP_L and BP shown similar registration errors when nine slices were used (see Table 1). This suggests that multiple SP_L acquisitions can have the same performance of multiple BP acquisitions, meaning that a 2D single-plane US with multiple slices can potentially achieve the same accuracy of 2D bi-plane US. However, the errors' variability was superior when using SP_L, which indicates that it is less repeatable than BP. Other researchers have tested the use of multiple slices in different approaches. Ahmad *et al.* reported a registration error of 0.8 mm [20]. However, tests were made in a kidney tumor phantom with 3 cm of width and 5 cm of length. In opposition, our tests were performed in a large model - porcine kidney phantoms with 5-7 cm and 10-13 cm of width and length, respectively, with a registration error of 1.80 mm (AVD for 9 slices SP_L, see Table 1). Likewise, Yu *et al.* concluded that multi-view 3D reconstructions from sparse 2D US images leaded to more accurate volume quantification compared to single views in cardiac images [39]. Similarly, Bogush *et al.* concluded, for simple objects, that 8 to 10 cross-sections were sufficient to obtain a mean volume error lower than 5% [40], which is consistent with our results (mean volume error ~9% for DSC). Nine slices presented on average the lowest registration errors, and the biplane, with pairs of slices (i.e. 18 slices), does not seem to considerably improve the registration accuracy.

As abovementioned, previous works have tried to register 2D US with CT or MRI for image-guided PRA based on surface-based registration. Mozer *et al.* considered rigid transformations between pre and intraoperative data, where CT and sparse 2D US (coupled to an optical tracker) images were used. They reported a repeatability and closed-loop accuracy of 0.79 mm and 1.2 mm, respectively [13]. However, no gold standard was available, and the authors tested the registration strategy using a single patient. Li *et al.* presented an orthogonal-ICP strategy using two pairs of orthogonal US images (aligned and parallel to transverse and longitudinal planes of the kidney), which were selected from sparse images at the maximum exhalation position. The results revealed a root-mean-square (RMS) target registration error of 3.53 mm in four healthy volunteers when fused with MRI data [12]. This result is close to our results when a similar number of slices were used during the registration process. Indeed, SP_L using five slices and BP using two slices (i.e. two pairs of orthogonal slices) presented an average P2P distance of 3.42 mm and 3.45 mm (for ICP2, see Table 1), respectively. Despite the interesting results, Li *et al.* required the use of an optical tracking based respiratory gating technique to obtain the maximum exhalation position. All steps were performed at this specific position, including image capture, registration, segmentation, and puncture. We believe that a safer interventional strategy should rely on the continuous monitoring of the kidney position based on US images. Li *et al.* also tested the same approach in a pig model, although using a statistical shape model (SSM) to three-dimensionally reconstruct the kidney, with a RMS error around 1 mm [14]. Thus, 3D kidney reconstruction from 2D US images has the potential to be used in image-guided PRA, and new strategies should be studied to improve these methodologies. The concept of 2D US with surface reconstruction has also been used for bone [41] and artery [42] interventions.

Regarding Hypothesis 3: *"Can different US probe's movements (acquiring kidney slices at different positions) benefit the final alignment between US and CT kidney surfaces?"*,

437 the results proved that different probe movements can give a better performance
438 during the registration process. The results suggested that yaw_{US} movements (i.e. a
439 sweep movement along the longitudinal view, see 3-I) leads to a better performance,
440 specifically for SP_L acquisitions (with an error of ~2 mm). This suggests that a single-
441 oriented sweep may obtain a valid alignment when 2D single-plane US acquisitions are
442 used. This can be relevant because 2D probes are more common in the urology field
443 than 4D ones. Although yaw_{US} movements using BP presented slightly higher errors
444 when compared with single-plane yaw_{US} motion, they had a lower IQR. It is relevant to
445 mention that yaw_{US} movements sliced the kidney equally for BP and SP_L. However, BP
446 differed on the presence of the central transverse plane. Therefore, this transverse
447 plane seems to positively affect the registration process by reducing the method's
448 sensitivity to the contours and initial alignment. In addition, the results presented in
449 Figure 5 revealed that when $roll_{CT}$, $pitch_{CT}$, and yaw_{CT} ranged between -50º and 50º,
450 the average errors were below 3 mm for the ICP2 method. As such, an initial and rough
451 pre-alignment of the preoperative data with the intraoperative one seems to be
452 mandatory for the ICP method. Among the two studied ICP methods, different
453 performances and error magnitudes were obtained throughout this study, as expected.
454 Previous studies revealed that the *point-to-plane* metric (i.e. ICP2) converges quicker
455 and, typically, with lower errors [32]. Figure 6 suggests that slicing the kidney along the
456 central longitudinal view may improve the registration. This may be related with the full
457 slicing of the longitudinal view that preserves more shape information of the kidney.

458 Overall, the results suggest that surface-based registration for image-guided PRA is a
459 valid strategy for intraoperative image registration, even from a single-oriented
460 acquisition. In addition to be a multi-modal approach, which can extend these results to
461 MRI for example, this approach has the potential to be applied to different
462 interventions. Indeed, the segmentation algorithm can be adapted for different
463 anatomical structures under intervention. In our study, although we studied only the

fusion based on the kidney surface, segmentation of internal structures [43] (such as renal calyx, renal medulla, renal cortex, renal column, etc.) and adjacent organs [44] (such as liver, intestines, vessels, etc.) may help improve the intraoperative fusion. However, future work must be performed to assess this hypothesis.

During the registration process, it was assumed rigid movements between tests, while scale, shear or nonrigid changes were disregarded. However, these can occur in real scenarios and can affect the alignment results, namely due to respiratory and small non-rigid movements of the tissues. This fact is one of the limitations of this study. Only a 4D US acquisition would provide the necessary information to manage the full set of possible transformations during image-guided PRA. As far as we know, currently, this information is not freely shared by manufacturers. Notwithstanding, as an advantage, 2D US data has usually better quality and higher amount of details than 3D/4D volume data, being a widely used tool in urological interventions. So, these reasons support why we still focus on 2D US imaging for multi-modal fusion. Therefore, the current findings are directly applicable in clinical practice, as long as real-time segmentation and registration algorithms are developed.

In summary, the results showed that SP_L and BP acquisitions had the best performance when multiple slices were used. The yaw_{US} movements, i.e. a large sweep along the central longitudinal view, presented the best results with an average error of ~2 mm.

In future, current strategy should be tested in an image-guided framework integrating automatic segmentation of both image modalities, an inter-modality registration strategy, tracking and puncture guidance in real-time.

5 CONCLUSIONS

This work assessed the optimal 2D US acquisition protocol to improve surface-based registration between CT and US data for image-guided PRA. It was observed that the use of contours from multiple planes and specific sweep movements of the US probes may be crucial to improve the final registration between CT and US data. Surface-based registration for image-guided PRA suggests being a valid strategy for intraoperative image fusion. This strategy has the potential to be applied to different image modalities and interventions, and the presented methodology has the potential to be used to assess their feasibility.

ACKNOWLEDGMENTS

The authors would like to thank the department of urology and department of imagiology of Hospital de Braga (Braga, Portugal).

FUNDING

This work has been funded by FEDER funds, through the Competitiveness Factors Operational Programme (COMPETE), and by National funds, through the Foundation for Science and Technology (FCT), under the scope of the project POCI-01-0145-FEDER-007038; and by the project NORTE-01-0145-FEDER-000013, supported by the Northern Portugal Regional Operational Programme (NORTE 2020), under the Portugal 2020 Partnership Agreement, through the European Regional Development Fund (FEDER).

João Gomes-Fonseca was funded by FCT under the Ph.D. grant PD/BDE/113597/2015.

The funders had no role in study design, data collection, and analysis, decision to publish, or preparation of the manuscript.

REFERENCES

1. Rosette J de la, Assimos D, Desai M, et al. The Clinical Research Office of the Endourological Society Percutaneous Nephrolithotomy Global Study: Indications, Complications, and Outcomes in 5803 Patients. *J Endourol*. 2011;25(1):11-17. doi:10.1089/end.2010.0424.

2. Knoll T, Michel MS, Alken P. Surgical atlas percutaneous nephrolithotomy: The Mannheim technique. *BJU Int*. 2007;99(1):213-231. doi:10.1111/j.1464-410X.2007.06613.x.

3. Liu Q, Zhou L, Cai X, Jin T, Wang K. Fluoroscopy versus ultrasound for image guidance during percutaneous nephrolithotomy: a systematic review and meta-analysis. *Urolithiasis*. 2017;45(5):481-487. doi:10.1007/s00240-016-0934-1.

4. de la Rosette JJMCH, Laguna MP, Rassweiler JJ, Conort P. Training in percutaneous nephrolithotomy--a critical review. *Eur Urol*. 2008;54(5):994-1001. doi:10.1016/j.eururo.2008.03.052.

5. Michel MS, Trojan L, Rassweiler JJ. Complications in percutaneous nephrolithotomy. *Eur Urol*. 2007;51(4):899-906. doi:10.1016/j.eururo.2006.10.020.

6. Rodrigues PL, Rodrigues NF, Fonseca J, Lima E, Vilaça JL. Kidney Targeting and Puncturing During Percutaneous Nephrolithotomy: Recent Advances and Future Perspectives. *J Endourol*. 2013;27(7):826-834. doi:10.1089/end.2012.0740.

7. Rodrigues PL, Vilaça JL, Oliveira C, et al. Collecting System Percutaneous Access Using Real-Time Tracking Sensors: First Pig Model In Vivo Experience. *J Urol*. 2013;190(5):1932-1937. doi:10.1016/j.juro.2013.05.042.

8. Lima E, Rodrigues PL, Mota P, et al. Ureteroscopy-assisted Percutaneous Kidney Access Made Easy: First Clinical Experience with a Novel Navigation System Using Electromagnetic Guidance (IDEAL Stage 1). *Eur Urol*. 2017;30(0):214-226. doi:10.1016/j.eururo.2017.03.011.

9. Ungi T, Beiko D, Fuoco M, et al. Tracked ultrasonography snapshots enhance needle

guidance for percutaneous renal access: a pilot study. *J Endourol*. 2014;28(9):1040-1045. doi:10.1089/end.2014.0011.

10. Leroy A, Mozer P, Payan Y, Troccaz J. Rigid Registration of Freehand 3D Ultrasound and CT-Scan Kidney Images. In: Barillot C, Haynor DR, Hellier P, eds. *Medical Image Computing and Computer-Assisted Intervention -- MICCAI 2004: 7th International Conference, Saint-Malo, France, September 26-29, 2004. Proceedings, Part I*. Berlin, Heidelberg: Springer Berlin Heidelberg; 2004:837-844. doi:10.1007/978-3-540-30135-6_102.

11. Wein W, Brunke S, Khamene A, Callstrom MR, Navab N. Automatic CT-ultrasound registration for diagnostic imaging and image-guided intervention. *Med Image Anal*. 2008;12(5):577-585. doi:10.1016/j.media.2008.06.006.

12. Li Z-C, Li K, Zhan H-L, Chen K, Gu J, Wang L. Augmenting intraoperative ultrasound with preoperative magnetic resonance planning models for percutaneous renal access. *Biomed Eng Online*. 2012;11(1):60-76. doi:10.1186/1475-925X-11-60.

13. Mozer P, Leroy A, Payan Y, Troccaz J, Chartier-Kastler E, Richard F. Computer-assisted access to the kidney. *Int J Med Robot Comput Assist Surg MRCAS*. 2005;1(4):58-66. doi:10.1002/rcs.58.

14. Li Z-C, Geng Niu, Li K, Zhan H-L, Yao-Qin Xie, Wang L. Augmented reality using 3D shape model for ultrasound-guided percutaneous renal access: A pig model study. In: *The 7th 2014 Biomedical Engineering International Conference*. IEEE; 2014:1-4. doi:10.1109/BMEiCON.2014.7017362.

15. Rodrigues PL, Moreira AHJ, Rodrigues NF, et al. Preliminary clinical trial in percutaneous nephrolithotomy using a real-time navigation system for percutaneous kidney access. In: Yaniv ZR, Holmes DR, eds. Vol 9036. International Society for Optics and Photonics; 2014:903606. doi:10.1117/12.2043647.

16. Rodrigues PL, Rodrigues NF, Fonseca JC, Vilaça JL. Validation of percutaneous puncture trajectory during renal access using 4D ultrasound reconstruction. In: Webster RJ, Yaniv ZR, eds. Vol 9415. International Society for Optics and Photonics;

2015:94152D. doi:10.1117/12.2082528.

17. Maintz JBAB, Viergever M a. A survey of medical image registration. *Med Image Anal*. 1998;2(1):1-36. doi:10.1016/S1361-8415(01)80026-8.

18. Viergever MA, Maintz JBA, Klein S, Murphy K, Staring M, Pluim JPW. A survey of medical image registration – under review. *Med Image Anal*. 2016;33:140-144. doi:10.1016/j.media.2016.06.030.

19. Alam F, Rahman SU, Ullah S, Gulati K. Medical image registration in image guided surgery: Issues, challenges and research opportunities. *Biocybern Biomed Eng*. 2018;38(1):71-89. doi:10.1016/J.BBE.2017.10.001.

20. Ahmad A, Cool D, Chew BH, Pautler SE, Peters TM. 3D segmentation of kidney tumors from freehand 2D ultrasound. In: Cleary KR, Galloway, Jr. RL, eds. Vol 6141. International Society for Optics and Photonics; 2006:61410S. doi:10.1117/12.653848.

21. Seo J, Koizumi N, Funamoto T, et al. Biplane US-Guided Real-Time Volumetric Target Pose Estimation Method for Theragnostic HIFU System. *J Robot Mechatronics*. 2011;23(3):400-407. doi:10.20965/jrm.2011.p0400.

22. Koizumi N, Seo J, Lee D, et al. Robust kidney stone tracking for a non-invasive ultrasound theragnostic system-Servoing performance and safety enhancement-. In: *2011 IEEE International Conference on Robotics and Automation*. IEEE; 2011:2443-2450. doi:10.1109/ICRA.2011.5980441.

23. Seo J, Koizumi N, Funamoto T, et al. Visual servoing for a US-guided therapeutic HIFU system by coagulated lesion tracking: a phantom study. *Int J Med Robot Comput Assist Surg*. 2011;7(2):237-247. doi:10.1002/rcs.394.

24. Seo J, Koizumi N, Mitsuishi M, Sugita N. Ultrasound image based visual servoing for moving target ablation by high intensity focused ultrasound. *Int J Med Robot*. 2017;13(4). doi:10.1002/rcs.1793.

25. Barbosa D, Dietenbeck T, Schaerer J, D'hooge J, Friboulet D, Bernard O. B-spline explicit active surfaces: an efficient framework for real-time 3-D region-based segmentation. *IEEE Trans Image Process*. 2012;21(1):241-251.

doi:10.1109/TIP.2011.2161484.

26. Queiros S, Morais P, Barbosa D, Fonseca JC, Vilaca JL, D'hooge J. MITT: Medical Image Tracking Toolbox. *IEEE Trans Med Imaging*. 2018:1-1. doi:10.1109/TMI.2018.2840820.

27. Shi L, Liu W, Zhang H, Xie Y, Wang D. A survey of GPU-based medical image computing techniques. *Quant Imaging Med Surg*. 2012;2(3):188-206. doi:10.3978/j.issn.2223-4292.2012.08.02.

28. Smistad E, Falch TL, Bozorgi M, Elster AC, Lindseth F. Medical image segmentation on GPUs – A comprehensive review. *Med Image Anal*. 2015;20(1):1-18. doi:10.1016/J.MEDIA.2014.10.012.

29. Gomes-Fonseca J, Miranda A, Morais P, et al. A Dual-Modal CT/US Kidney Phantom Model for Image-Guided Percutaneous Renal Access. In: Springer, Cham; 2018:378-387. doi:10.1007/978-3-319-68195-5_42.

30. Horn BKP. Closed-form solution of absolute orientation using unit quaternions. *J Opt Soc Am A*. 1987;4(4):629. doi:10.1364/JOSAA.4.000629.

31. Chu C, Masic S, Usawachintachit M, et al. Ultrasound-Guided Renal Access for Percutaneous Nephrolithotomy: A Description of Three Novel Ultrasound-Guided Needle Techniques. *J Endourol*. 2016;30(2):153-158. doi:10.1089/end.2015.0185.

32. Rusinkiewicz S, Levoy M. Efficient variants of the ICP algorithm. *Proc Int Conf 3-D Digit Imaging Model 3DIM*. 2001:145-152. doi:10.1109/IM.2001.924423.

33. Besl PJ, Mckay HD. A method for registration of 3-D shapes. *Pattern Anal Mach Intell IEEE Trans*. 1992;14:239-256. doi:10.1109/34.121791.

34. Segal A, Haehnel D, Thrun S. Generalized-ICP. In: *Proceedings of Robotics: Science and Systems*. ; 2009:1-8. doi:10.15607/RSS.2009.V.021.

35. Bellekens B, Spruyt V, Weyn M. A Survey of Rigid 3D Pointcloud Registration Algorithms. In: *AMBIENT 2014, The Fourth International Conference on Ambient Computing, Applications, Services and Technologies. 2014.* ; 2014:8-13.

624 36. Bellekens B, Spruyt V, Berkvens R, Penne R, Weyn M. A Benchmark Survey of Rigid 3D
625 Point Cloud Registration Algorithms. *Int J Adv Intell Syst*. 2015;8(1):118-127.
626 http://www.iariajournals.org/intelligent_systems/.

627 37. Lang P, Chu MWA, Bainbridge D, Guiraudon GM, Jones DL, Peters TM. Surface-based
628 CT-TEE registration of the aortic root. *IEEE Trans Biomed Eng*. 2013;60(12):3382-3390.
629 doi:10.1109/TBME.2013.2249582.

630 38. Lang P, Rajchl M, Li F, Peters TM. Towards model-enhanced real-time ultrasound
631 guided cardiac interventions. In: *Proceedings - 2011 International Conference on*
632 *Intelligent Computation and Bio-Medical Instrumentation, ICBMI 2011*. ; 2011:89-92.
633 doi:10.1109/ICBMI.2011.24.

634 39. Yu H, Pattichis MS, Agurto C, Beth Goens M. A 3D Freehand Ultrasound System for
635 Multi-view Reconstructions from Sparse 2D Scanning Planes. *Biomed Eng Online*.
636 2011;10. doi:10.1186/1475-925X-10-7.

637 40. Bogush AL, Tuzikov A V. 3D Object Volume Measurement Using Freehand Ultrasound.
638 In: Kalviainen H, Parkkinen J, Kaarna A, eds. *Image Analysis*. Berlin, Heidelberg:
639 Springer Berlin Heidelberg; 2005:1066-1075.

640 41. Ciganovic M, Ozdemir F, Pean F, Fuernstahl P, Tanner C, Goksel O. Registration of 3D
641 freehand ultrasound to a bone model for orthopedic procedures of the forearm. *Int J*
642 *Comput Assist Radiol Surg*. 2018;13(6):827-836. doi:10.1007/s11548-018-1756-0.

643 42. Smistad E, Lindseth F. Real-Time Automatic Artery Segmentation, Reconstruction and
644 Registration for Ultrasound-Guided Regional Anaesthesia of the Femoral Nerve. *IEEE*
645 *Trans Med Imaging*. 2016;35(3):752-761. doi:10.1109/TMI.2015.2494160.

646 43. Torres HR, Queirós S, Morais P, Oliveira B, Fonseca JC, Vilaça JL. Kidney
647 segmentation in ultrasound, magnetic resonance and computed tomography images: A
648 systematic review. *Comput Methods Programs Biomed*. 2018;157:49-67.
649 doi:10.1016/j.cmpb.2018.01.014.

650 44. Oliveira B, Queirós S, Morais P, et al. A novel multi-atlas strategy with dense
651 deformation field reconstruction for abdominal and thoracic multi-organ segmentation

652 from computed tomography. *Med Image Anal*. 2018;45:108-120.
653 doi:10.1016/j.media.2018.02.001.

654